

1 **The *in vitro* antiviral activity of the anti-hepatitis C virus (HCV) drugs daclatasvir and**
2 **sofosbuvir against SARS-CoV-2**

3 Running-title: SARS-CoV-2 susceptibility to daclatasvir *in vitro*

4 Carolina Q. Sacramento^{1,12#}, Natalia Fintelman-Rodrigues^{1, 12#}, Jairo R. Temerozo^{2,3}, Aline
5 de Paula Dias Da Silva^{1,12}, Suelen da Silva Gomes Dias¹, Carine dos Santos da Silva^{1,12},
6 André C. Ferreira^{1,4,12}, Mayara Mattos^{1,12}, Camila R. R. Pão¹, Caroline S. de Freitas^{1, 12},
7 Vinicius Cardoso Soares¹, Lucas Villas Bôas Hoelz⁵, Tácio Vinícius Amorim Fernandes^{5,6},
8 Frederico Silva Castelo Branco⁵, Mônica Macedo Bastos⁵, Núbia Boechat⁵, Felipe B.
9 Saraiva⁷, Marcelo Alves Ferreira^{7,12}, Rajith K. R. Rajoli⁸, Carolina S. G. Pedrosa⁹, Gabriela
10 Vitória⁹, Letícia R. Q. Souza⁹, Livia Goto-Silva⁹, Marilia Zaluar Guimarães^{9,10}, Stevens K.
11 Rehen^{9,10}, Andrew Owen⁸, Fernando A. Bozza^{9,11}, Dumith Chequer Bou-Habib^{2,3}, Patrícia T.
12 Bozza¹, Thiago Moreno L. Souza^{1,12,*}

13 # - These authors contributed equally to this work

14

15 1 – Laboratório de Imunofarmacologia, Instituto Oswaldo Cruz (IOC), Fundação Oswaldo
16 Cruz (Fiocruz), Rio de Janeiro, RJ, Brazil.

17 2 – National Institute for Science and Technology on Neuroimmunomodulation
18 (INCT/NIM), IOC, Fiocruz, Rio de Janeiro, RJ, Brazil.

19 3 – Laboratório de Pesquisas sobre o Timo, IOC, Fiocruz, Rio de Janeiro, RJ, Brazil.

20 4 - Universidade Iguáçu, Nova Iguáçu, RJ, Brazil.

21 5 – Instituto de Tecnologia de Fármacos (Farmanguinhos), Fiocruz, Rio de Janeiro, RJ,
22 Brazil.

23 6 – Laboratório de Macromoléculas, Diretoria de Metrologia Aplicada às Ciências da
24 Vida, Instituto Nacional de Metrologia, Qualidade e Tecnologia - INMETRO, Duque de
25 Caxias, RJ 25250-020, Brazil

26 7 - Instituto de Tecnologia em Imunobiológicos (Bio-Manguinhos), Fiocruz, Rio de
27 Janeiro, RJ, Brazil

28 8 - Department of Molecular and Clinical Pharmacology, University of Liverpool, Liverpool,
29 L7 3NY, UK;

30 9 – Instituto D’Or de Pesquisa e Ensino, Rio de Janeiro, RJ, Brazil

31 10 - Instituto de Ciências Biomédicas, Universidade Federal do Rio de Janeiro, Rio de
32 Janeiro, RJ, Brazil.

33 11 - Instituto Nacional de Infectologia Evandro Chagas, Fiocruz, Rio de Janeiro, RJ, Brazil

34 12 - National Institute for Science and Technology on Innovation in Diseases of Neglected
35 Populations (INCT/IDPN), Center for Technological Development in Health (CDTS),
36 Fiocruz, Rio de Janeiro, RJ, Brazil.

37

38

39 *Correspondence footnote:

40 Thiago Moreno L. Souza, PhD

41 *****

42 Fundação Oswaldo Cruz (Fiocruz)

43 Centro de Desenvolvimento Tecnológico em Saúde (CDTS)

44 Instituto Oswaldo Cruz (IOC)

45 Pavilhão Osório de Almeida, sala 16

46 Av. Brasil 4365, Manguinhos, Rio de Janeiro - RJ, Brasil, CEP 21060340

47 Tel.: +55 21 2562-1311

48 Email: tmoreno@cdts.fiocruz.br

49 **Abstract**

50 Current approaches of drugs repurposing against 2019 coronavirus disease (COVID-19)
51 have not proven overwhelmingly successful and the severe acute respiratory syndrome
52 coronavirus 2 (SARS-CoV-2) pandemic continues to cause major global mortality.
53 Daclatasvir (DCV) and sofosbuvir (SFV) are clinically approved against hepatitis C virus
54 (HCV), with satisfactory safety profile. DCV and SFV target the HCV enzymes NS5A and
55 NS5B, respectively. NS5A is endowed with pleotropic activities, which overlap with several
56 proteins from SARS-CoV-2. HCV NS5B and SARS-CoV-2 nsp12 are RNA polymerases
57 that share homology in the nucleotide uptake channel. We thus tested whether SARS-CoV-
58 2 would be susceptible these anti-HCV drugs. DCV consistently inhibited the production of
59 infectious SARS-CoV-2 in Vero cells, in the hepatoma cell line (HuH-7) and in type II
60 pneumocytes (Calu-3), with potencies of 0.8, 0.6 and 1.1 μ M, respectively. Although less
61 potent than DCV, SFV and its nucleoside metabolite inhibited replication in Calu-3 cells.
62 Moreover, SFV/DCV combination (1:0.15 ratio) inhibited SARS-CoV-2 with EC₅₀ of 0.7:0.1
63 μ M in Calu-3 cells. SFV and DCV prevented virus-induced neuronal apoptosis and release
64 of cytokine storm-related inflammatory mediators, respectively. Both drugs inhibited
65 independent events during RNA synthesis and this was particularly the case for DCV, which
66 also targeted secondary RNA structures in the SARS-CoV-2 genome. Concentrations
67 required for partial DCV *in vitro* activity are achieved in plasma at Cmax after administration
68 of the approved dose to humans. Doses higher than those approved may ultimately be
69 required, but these data provide a basis to further explore these agents as COVID-19 antiviral
70 candidates.

71

72

73

74

75

76

77

78

79

80

81

82

83

84

85 1) Introduction

86 In these two decades of the 21st century, life-threatening public health emergencies
87 were related to highly pathogenic coronaviruses (CoV), such as severe acute respiratory
88 syndrome (SARS-CoV) in 2002, middle-east respiratory syndrome (MERS-CoV) in 2014[1]
89 and SARS-CoV-2 contemporaneously. After 8 months of the 2019 CoV disease (COVID-
90 19) outbreak, 15 million cases and over 750 thousand deaths were confirmed[2].

91 To specifically combat COVID-19, the World Health Organization (WHO) launched
92 the global Solidarity trial, initially composed of lopinavir (LPV)/ritonavir (RTV), combined
93 or not with interferon- β (IFN- β), chloroquine (CQ) and remdesivir (RDV) [3]. Lack of
94 clinical benefit paused the enthusiasm for CQ, its analogue hydroxychloroquine and
95 LPV/RTV against COVID-19[4–6]. RDV showed promising results in non-human primates
96 and clinical studies during early intervention[5,7,8]. Nevertheless, RDV's access may be
97 limited due to its price, and the necessity of intravenous use makes early intervention
98 impracticable and complicates feasibility within many healthcare settings.

99 Direct-acting antivirals (DDA) against hepatitis C virus (HCV) are among the safest
100 antiviral agents, since they become routinely used in the last five years[9]. Due to their recent
101 incorporation among therapeutic agents, drugs like daclatasvir (DCV) and sofosbuvir (SFV)
102 have not been systematically tested against SARS-CoV or MERS-CoV.

103 DCV inhibits HCV replication by binding to the N-terminus of non-structural protein
104 (NS5A), affecting both viral RNA replication and virion assembly[10]. NS5A is a
105 multifunctional protein in the HCV replicative cycle, involved with recruitment of host
106 cellular lipid droplets, RNA binding and replication, protein-phosphorylation, cell signaling
107 and antagonism of interferon pathways[10]. In large positive sense RNA viruses, such as
108 SARS-CoV-2, these activities are executed by various viral proteins, especially the non-
109 structural proteins (nsp) 1 to 14[11]. SFV inhibits the HCV protein NS5B, its RNA
110 polymerase[12]. This drug has been associated with antiviral activity against other positive
111 sense RNA viruses, such as Zika (ZIKV), yellow fever (YFV) and chikungunya (CHIKV)
112 viruses [13–16]. With respect to HCV, SFV appears to have a high barrier to the
113 development of resistance. SFV is 2'Me-F uridine monophosphate nucleotide[12].
114 Hydrophobic protections in its phosphate allow SFV to enter the cells, and then this pro-drug
115 must become the active triphosphorylated nucleotide. Although the cellular enzymes
116 cathepsin A (CatA), carboxylesterase 1 (CES1) and histidine triad nucleotide-binding protein
117 1 (Hint1) involved with removal of monophosphate protections are classically associated
118 with the hepatic expression[17], they are also present in other tissue, such as the respiratory
119 tract [18–20]. Moreover, the similarities between the SARS-CoV-2 and HCV RNA
120 polymerase provide a rational for studying sofosbuvir as an antiviral for COVID-19 [21].
121 Using enzymatic assays, sofosbuvir was shown to act as a competitive inhibitor and a chain
122 terminator for SARS-CoV-2 RNA polymerase[22,23]. In human brain organoids, SFV
123 protected neural cells from SARS-CoV-2-induced cell death [24].

124 Taken collectively, current data provided a bases to investigate whether DCV and
125 SFV could inhibit the production of infectious SARS-CoV-2 particles in physiologically

126 relevant cells. DCV consistently inhibited the production of infectious SARS-CoV-2 in
127 different cells, impairing virus RNA synthesis with an apparently novel mechanism of action,
128 by targeting double-stranded viral RNA. DCV also prevented the release of the inflammatory
129 mediators IL-6 and TNF- α , which are associated with COVID-19 cytokine storm, in SARS-
130 CoV-2-infected primary human monocytes. SFV, which was inactive in Vero cells, inhibited
131 SARS-CoV-2 replication more potently in hepatoma than in respiratory cells. Furthermore,
132 SFV potency appeared to be augmented in the presence of sub-inhibitory concentrations of
133 DCV. These data support further investigation of DCV/SFV for COVID-19. Of interest,
134 concentrations providing sub-maximal inhibition of SARS-CoV-2 by DCV are achieved in
135 plasma at maximal concentration (Cmax) after administration of its approved dose of 60mg
136 once daily, which has considerable scope for dose escalation.

137

138 2) Results

139 2.1) DCV is more potent than SFV to inhibit the production of infectious SARS-CoV-2 140 particles.

141 SARS-CoV-2 may infect cell lineages from different organs, but permissive
142 production of infectious virus particles varies according to the cellular systems. Since we
143 wanted to diminish infectious virus titers with studied antiviral drugs, we first compared cell
144 types used in SARS-CoV-2 research with respect to their permissiveness to this virus.
145 Whereas African green monkey kidney cell (Vero E6), human hepatoma (HuH-7) and type
146 II pneumocytes (Calu-3) produced infectious SARS-CoV-2 titers and quantifiable RNA
147 levels (Figure S1), A549 pneumocytes and induced pluripotent human neural stem cells
148 (NSC) displayed limited ability to generate virus progeny, as measured by plaque forming
149 units (PFU) of virus below the limit of detection (Figure S1A).

150 Next, the phenotypic experiments were performed at MOI of 0.01 for Vero cells 24h after
151 infection, and 0.1 for HuH-7 and Calu-3 cells at 48h after infection. Cultures were treated
152 after 1h infection period and cell culture supernatant fractions were harvested to measure
153 infectious SARS-CoV-2 by plaque forming units (PFUs) in Vero cells. DCV consistently
154 inhibited the production of SARS-CoV-2 infectious virus titers in a dose-dependent manner
155 in the all tested cell types (Figure 1), being similarly potent in Vero, HuH-7 and Calu-3 cells,
156 with EC₅₀ values ranging between 0.6 to 1.1 μ M, without statistical distinction (Table 1).
157 DCV showed limited antiviral activity when viral RNA copies/mL in the culture supernatant
158 fraction (Figures S2) was utilized, suggesting a mechanism unrelated to RNA production.

159 SARS-CoV-2 susceptibility to SFV in Huh-7 and Calu-3 cells was lower compared
160 to DCV (Figure 1B and D and Table 1). Because vero cells poorly activate SFV to its active
161 triphosphate, SFV did not affect SARS-CoV-2 replication in these cells. Similarly, to what
162 was observed for DCV, quantification of SFV's antiviral activity by PFUs was more sensitive
163 than by viral RNA quantification in the supernatant fraction (Figure S2). DCV was at least
164 7-times more potent than SFV in HuH-7 and Calu-3 cells (Table 1).

165 SFV's nucleoside metabolite (GS-331007) was also tested for anti-SARS-CoV-2
166 activity. GS-331007 was inactive in Vero cells and less active than SFV in Huh-7 cells

167 (Figure 1 and Table 1). Curiously, in respiratory cells, GS-331007 presented a moderate anti-
168 SARS-CoV-2 activity, similar to that of SFV (Figure 1 and Table 1).

169 Given that SARS-CoV-2 replication in Calu-3 cells appeared to be more sensitive to
170 antiviral activity, this cell line was used to assess the combination of SFV and DCV.
171 SFV/DCV combination was used at a ratio of 1:0.15 ratio, in accordance with its dose ratio
172 for HCV-positive patients (400 mg SFV plus 60 mg DCV). In this assessment of the
173 interaction, the potency of SFV increased 10-fold in the presence of suboptimal DCV
174 concentrations (Figure 1C and E and Table 1).

175 DCV was demonstrated to be 1.1- to 4-fold more potent than the positive controls
176 CQ, LPV/RTV and ribavirin (RBV) (Figures 1 and Table 1), whereas SFV potency was
177 similar to that of RBV in HuH-7 and Calu-3 cells (Figures 1 and Table 1). However, the
178 selectivity index ($SI = CC_{50}/EC_{50}$) for SFV was 4.6-fold superior to RBV, because of SFV's
179 lower cytotoxicity (Table 1). None of the studied drugs were more potent than RDV (Figure
180 1 and Table 1).

181 These data demonstrate that SARS-CoV-2 is susceptible to DCV and SFV *in vitro*,
182 with a higher potency demonstrated for DCV.

183

184 **2.2 Protective effect of SFV and DCV in non-permissive cells**

185 Although productive replication in neurons and monocytes was not observed (Figure
186 S1), infection of these cells is known to be associated with neuro-COVID-19[25] and
187 cytokine storm[26], respectively. Therefore, these cell types may be important targets for
188 repurposed antiviral drugs.

189 SFV reduced SARS-CoV-2 RNA levels by 20 - 40% in NSCs, at a concentration of 1
190 μ M (Figure 2A). Conversely, no impact of DCV on SARS-CoV-2 RNA levels were observed
191 in NSC (Figure 2A), consistently with the other cell types assayed (Figure S2). Using the
192 more complex system of NSC-based neurospheres, the number of tunel-positive nuclei over
193 total nuclei as a proxy of apoptotic cells was assessed. SFV completely prevented SARS-
194 CoV-2-induced apoptosis (Figure 2B), whereas benefits of DCV in this system were limited.

195 In SARS-CoV-2-infected human primary monocytes, 1 μ M DCV reduced viral RNA
196 levels/cell (Figure 3A), whereas SFV was inactive. DCV also reduced the SARS-CoV-2-
197 induced enhancement of TNF- α and IL-6 (Figure 3B and C). These data provide further
198 evidence for a putative benefit in COVID-19 with the investigated HCV DDAs if target
199 concentrations can be achieved in patients.

200 SFV and DCV cooperatively target virus replication in cells from different anatomical
201 sites, preventing SARS-CoV-2-mediated neuronal cell death and the increase of pro-
202 inflammatory mediators.

203

204 **2.3 DCV and SFV may target different events during SARS-CoV-2 RNA synthesis.**

205 The observation that suboptimal concentrations of DCV augmented antiviral activity
206 of SFV (Figure 1C and F) may indicate that they target different processes during viral
207 replication. As a nucleotide analog, SFV was described to competitively inhibit the SARS-
208 CoV-2 RNA polymerase[22]. In HCV, DCV blocks the multi-functional protein NS5A, also
209 suggesting these agents target different mechanisms within the SARS-CoV-2 life cycle. To
210 gain insights on the temporality of DCV's activity against SARS-CoV-2, Vero cells were

211 infected at MOI of 0.01 and treated at different timepoints, with DCV at 2-fold its EC₅₀. This
212 time-of-addition assay demonstrated that DCV treatment could be efficiently postponed up
213 to 4 h, similarly to RBV, a pan-RNA polymerase inhibitor (Figure 4A). These results suggest
214 that inhibition of viral RNA synthesis is the limiting event targeted by DCV.

215 To confirm the rational that both SFV and DCV inhibit viral RNA synthesis in
216 physiologically relevant cells, intracellular levels of SARS-CoV-2 genomic and subgenomic
217 RNA were measured in type II pneumocytes, Calu-3 cells. A two-fold higher inhibition of
218 viral RNA synthesis was observed for DCV compared to SFV (Figure 4B), when both were
219 tested at 10 μ M. SFV/DCV cooperatively inhibited SARS-CoV-2 RNA synthesis, even at
220 1 μ M, also supporting different targets for each agent during replicase activity.

221 Molecular docking methods were applied to predict the complexes with lowest energy
222 interactions between the SARS-CoV-2 RNA polymerase and the active metabolite of SFV
223 as well as DCV. The SFV active metabolite and DCV presented rerank score values of -74.09
224 a.u. and -84.64 a.u., respectively. In addition, the hydrogen bonds (H-bonds), attractive
225 electrostatic, and steric interactions were mapped using a ligand-map algorithm[27]. The SFV
226 active metabolite was predicted to interact via hydrogen bonds (H-bond) with Arg553, Cys622,
227 Asp623, and Asn691 residues and with U20 RNA nucleotide (H-bond interaction energy = -
228 3.50 u.a.), also presenting electrostatic interactions with Lys551, Arg553, and with the two
229 Mg²⁺ ions (electrostatic interaction energy = -13.14 u.a.), as described by Gao coworkers[21],
230 and steric interactions with Arg553, Cys622, Asp623, and Asn691 residues (steric interaction
231 energy = -74.09 u.a.) (Figure 5A and C). Furthermore, these predictions indicated that DCV
232 may interact with viral RNA in the cleft of the SARS-CoV-2 RNA polymerase (Figure 5B
233 and D), with anchoring through H-bonds with Tyr546 and Thr687 residues, and with U9
234 RNA nucleotide (H-bond interaction energy = 3.68 u.a.), and also showing steric interactions
235 with Tyr546 and Thr687 residues (steric interaction energy = -84.64 u.a.) (Figure 5B and D).

236

237 **2.4) DCV effect on SARS-CoV-2 RNA**

238 Predictions from molecular modeling and data from in vitro phenotypic assays
239 suggested that DCV could target SARS-CoV-2 RNA synthesis. Therefore, a melting curve
240 of extracted viral RNA was generated to assess whether DCV could affect the virus RNA
241 folding. SARS-CoV-2 RNA displays secondary structures throughout its sequence, which
242 are important during viral replication and transcription[28], which can be monitored through
243 melting curve analysis using a regular real time thermocycler. The thermal melting profiles
244 of the RNA and RNA/DCV complexes, obtained by varying the temperature, showed
245 concentration-dependent effects favoring denaturation of the nucleic acid at low temperatures
246 (Figure 6A and B).

247 In order to investigate further, it was hypothesized that continuous culture of the virus
248 in the presence of DCV may result in mutations in the SARS-CoV-2 RNA which change the
249 pattern of secondary structure. Following two months successive passage of the virus in Vero
250 cells at the MOI of 0.1 in the presence of increasing concentrations, a 30% mutant
251 subpopulation was detected in the presence of 7 μ M DCV (Figure 6C). A putative secondary
252 structure at positions 28169-28259 of the SARS-CoV-2 genome was changed in the mutant
253 virus (yielded in the presence of DCV) in comparison to wild-type (SARS-CoV-2 virus
254 grown in parallel without treatment) (Table 2, Figure 6D and E, genbank #MT827075,

255 MT827190, MT827872, MT827940, MT827074, MT827202, MT835026, MT835027,
256 MT835383, SRR12385359 and its coverage in Figure S3). The positions 28169-28259 are
257 located at the junction between ORF8 and N gene; thus, the change in the shape of the
258 secondary RNA structure may prevent the binding of specific components required for the
259 transcription of these genes (Figure 6D and E). Moreover, the low sequence identity of the
260 mutant with SARS-CoV-2 genomes in genbank suggests that it may be unlikely that mutant
261 virus possesses adequate fitness (Table 2), which is in line with the observed reduction in
262 virus infectious titers.

263

264 **2.5) Physiologically based pharmacokinetic (PBPK) modelling for DCV**

265 A recent analysis of drugs proposed for repurposing as SARS-CoV-2 antiviral medicines
266 revealed that very few of the proposed candidates achieved their target concentrations after
267 administration of approved doses to humans [29]. Moreover, there have been several recent
268 calls to integrate understanding of pharmacokinetic principles into COVID-19 drug
269 prioritization[30–32]. Initial assessment of the plasma pharmacokinetics of SFV indicated
270 that the concentrations able to inhibit SARS-CoV-2 replication in vitro were unlikely to be
271 achievable after approved doses. However, inhibitory DCV concentrations were close to
272 those achieved following administration of its approved HCV dose. Therefore,
273 Physiologically based pharmacokinetic (PBPK) modelling was used to estimate the dose and
274 schedule of this drug to maximize the probability of success for COVID-19.

275 PBPK model validation against various single and multiple oral doses of DCV had a ratio
276 <2 between mean simulated and observed values and a summary of this shown in
277 supplementary tables S1 and 2. The average absolute fold error (AAFE) values for the
278 observed vs simulated plasma concentration – time curve for a single 100 mg dose and
279 multiple 60 mg OD doses were 0.92 and 0.76, respectively, and are shown in supplementary
280 figure S4 and S5. Thus, the known pharmacokinetic values and plots are in the agreeable
281 range for the DCV PBPK model to assumed as validated.

282 Supplementary figures S6 and S7 show the C_{24} values for various BID and TID dose
283 simulations, and 540 mg BID and 330 mg TID were shown to satisfy systemic concentrations
284 above the EC₉₀ for at least 90% of the simulated population. Optimal dose was identified to
285 be 330 mg TID as this dosing regimen requires lower dose per day than 540 mg BID. A
286 comparison between 60 mg TID and 330 mg TID daclatasvir is shown in Figure 7 that satisfy
287 C_{24} for EC₅₀ (0.8 μ M, 591 ng/ml) and EC₉₀ respectively for treatment of SARS-CoV-2.

288 3) Discussion

289 The COVID-19 pandemic continues to present a major concern to global health, and is
290 the most significant economic threat in decades[33]. Less than 8 months after the outbreak
291 in Wuhan, China, the WHO recorded more 750,000 deaths worldwide¹. SARS-CoV-2 is the
292 third highly pathogenic coronavirus that emerged in the two decades of the 21st century,
293 following SARS-CoV and MERS-CoV[1]. SARS-CoV-2 actively replicates in type II
294 pneumocytes, leading to cytokine storm and the exacerbation of thrombotic
295 pathways[26,34,35]. Besides the virus-triggered pneumonia and sepsis-like disease
296 associated with severe COVID-19, SARS-CoV-2 may reach the central nervous system[25]
297 and liver[36]. Early blockage of the natural clinical evolution of infection by antivirals will
298 likely prevent the disease progression to severe COVID-19[26,34,35]. Indeed, clinical
299 studies providing early antiviral intervention accelerated the decline of viral loads and slowed
300 disease progression[7,8]. The decrease of viral loads is likely to be a critical laboratory
301 parameter, because lowering viral shedding may protect the individual and reduced
302 transmissibility is likely to have population-level benefits.

303 To rapidly respond to unfolding pandemics, the cataloguing of preclinical data on
304 susceptibility of SARS-CoV-2 to approved drugs is of paramount importance, and provides
305 opportunities for rational selection of promising products for evaluation in clinical trials [37].
306 The investigators used this approach during ZIKV, YFV, and CHIKV outbreak in Brazil, and
307 demonstrated susceptibility of these viruses to SFV [13–16,38]. SFV and DCV are
308 considered safe and well tolerated anti-HCV therapies that are orally bioavailable. The
309 presented work demonstrates: i) SARS-CoV-2 is susceptible to DCV, ii) DCV/SFV co-
310 treatment show cooperative antiviral effect on SARS-CoV-2 replication in respiratory cells;
311 iii) SFV and DCV prevented virus-induced neuronal apoptosis and release of cytokine storm-
312 related mediators in monocytes, respectively; iv) DCV and SFV inhibited independent events
313 during RNA synthesis; v) DCV favors the unfold of SARS-CoV-2 secondary RNA
314 structures, and vi) target concentration of DCV set by the *in vitro* activities are within the
315 range that may be achievable in humans.

316 In the 9.6 kb genome of HCV, the gene *ns5a* encodes for a multifunctional protein. The
317 protein NS5A possesses motifs involved with lipid, zinc and RNA binding, phosphorylation
318 and interaction with cell signaling events[10]. In other viruses, with less compact genomes,
319 the functions and motifs present in NS5A are distributed to other proteins. For instance, in
320 SARS-CoV-2, its 29 kb genome encodes for nsp3, with zinc motif; nsp4 and 5, with lipidic
321 binding activity; nsp7, 8, 12, 13 and 14 able to bind RNA[11]. Although there is not a specific
322 orthologue of NS5A in the SARS-CoV-2 genome, their activities may be exerted by multiple
323 other proteins. DCV inhibited the production of infectious SARS-CoV-2 titers with EC₅₀
324 values ranging from 0.6 to 1.1 μM across different cell types, including pneumocytes.
325 Curiously, DCV's antiviral activity was not exhibited when virus replication was accessed
326 by quantifying viral RNA loads. Our sub-sequential analysis illustrated that DCV mechanism
327 of action could be, at least in part, associated with targeting viral RNA secondary structures,
328 in line with the observation of lower infectivity in the absence of viral RNA decline in culture
329 supernatant. SARS-CoV-2 possesses RNA pseudoknots that could contribute to the

330 transcription processes[28], and DCV-associated denaturation of these structures could limit
331 viral RNA polymerase activity. This already impaired catalysis may promote cooperative
332 activity of SFV.

333 With relevance to SFV, the homology of the new-2019-CoV and HCV orthologue
334 enzyme were confirmed [21]. In enzyme kinetic assays with SARS-CoV-2 nsp7, 8 and 12,
335 the SARS-CoV-2 RNA polymerase complex, SFV-triphosphate, the active metabolite,
336 competitively acts as a chain terminator[22,23]. Similarly, RBV-, favipiravir- and RDV-
337 triphosphate also target SARS-CoV-2 RNA elongation[22,23]. Indeed, SFV reduced the
338 RNA synthesis in SARS-CoV-2-infected cells able to convert the pro-drug to its active
339 triphosphate, such as hepatoma cells. This activation process requires a multi-stage pathway
340 in which hydrophobic protections in the SFV monophosphate are removed by the cellular
341 enzymes CatA, CES1 and HINT, with subsequent followed by engagement of nucleoside
342 monophosphate and diphosphate kinase [17]. According to the Human Protein Atlas, these
343 enzymatic entities are also found in the respiratory tract[18–20]. Indeed, we found that
344 SARS-CoV-2 replication could be inhibited by SFV at high concentration, not only in
345 hepatoma cells – but also in Calu-3 type II pneumocytes. Interestingly, RDV, which shares
346 structural characteristics with SFV, such as to be converted from the ProTide/prodrug to
347 active metabolite, is active in the respiratory tract[39]. Moreover, there is a body of evidence
348 suggesting that the ProTide phosphoramidate protections would be dispensable from RDV in
349 respiratory cells because the nucleoside analog, GS-441524, is active against human and
350 feline CoV [39–41]. Since there are open questions on the efficiency in which respiratory
351 cells convert nucleosides to nucleotides, the nucleoside version of SFV (GS-331007) was
352 tested against SARS-CoV-2. GS-331007 was virtually inactive in all cell types except for
353 Calu-3, in which it exerted similar activity to SFV. Importantly, GS-331007 has broader
354 distribution in anatomical compartments than SFV, which may be important in the context
355 of anatomical target-site activity.

356 Considering that DCV could favor RNA denaturation, conformational changes in the
357 viral RNA template/primer dimer at nsp12 active site may limit efficiency or processing by
358 this enzyme. Since SARS-CoV-2 RNA polymerase kinetics is impaired by DCV, SFV could
359 be less impacted by hindrance via amino acid Asp623[22] in this enzyme. This hypothesis
360 warrants further investigation to confirm the mechanistic-basis for the possible cooperation
361 between SFV and DCV *in vitro* model, and clinically if observations from recent trials are
362 confirmed[42].

363 SFV was able to prevent apoptosis in human neurons, whereas DCV prevented the
364 enhancement of IL-6 and TNF- α levels in human monocytes. These secondary mechanisms
365 may also support cooperativity between SFV and DCV, because neurological SARS-CoV-2
366 infection and cytokine storm are associated with poor clinical outcomes[25,26]. Another
367 study also reported that SFV could be protective against neuro-COVID *in vitro*[24].
368 However, the authors analyzed only a single dose of 20 μ M, which greatly exceeds the
369 concentrations achieved by SFV after approved dosing to humans [17]. Here,
370 neuroprotection is demonstrated to be promoted by SFV at 1 μ M, which is closer to
371 physiological concentrations [17].

372 Based upon targets set by the *in vitro* pharmacological activity of DCV, PBPK modelling
373 indicated that systemic concentrations able to inhibit SARS-CoV-2 may be achievable in
374 humans. Dose escalation may be needed to provide fully suppressive concentrations across
375 the entire dosing interval, as has been shown to be needed for other viruses. However, the
376 validity of such an approach would require careful assessment of safety and tolerability
377 through phase I evaluation of the higher doses. Furthermore, the prerequisite
378 pharmacokinetic-pharmacodynamic relationships for successful anti-SARS-CoV-2 activity
379 are yet to be unraveled, and will likely require better understanding of the target-site
380 penetration and free drug concentrations in matrices that recapitulate relevant compartments.
381 Notwithstanding, the approved dose of DCV (60mg OD) is low in relationship to other
382 antiviral agents, and the PBPK model provides posologies that may be reachable in dose-
383 escalation trials.

384 In summary, effective early antiviral interventions are urgently required for the SARS-
385 CoV-2 pandemic to improve patient clinical outcomes and disrupt transmission at population
386 level. The presented data for two widely available anti-HCV drugs, particularly for DCV,
387 provide a rational basis for further validation of these molecules for anti-SARS-CoV-2
388 interventions.

389

390 4) Material and Methods

391 4.1. Reagents

392 The antivirals RDV and LPV/RTV (4:1 proportion) was purchased from Selleckchem
393 (<https://www.selleckchem.com/>). Chloroquine and ribavirin were received as donations from
394 Instituto de Tecnologia de Fármacos (Farmanguinhos, Fiocruz). DCV and SFV were donated
395 by Microbiologica Química-Farmacêutica LTDA (Rio de Janeiro, Brazil). ELISA assays
396 were purchased from R&D Bioscience. All small molecule inhibitors were dissolved in 100%
397 dimethylsulfoxide (DMSO) and subsequently diluted at least 10⁴-fold in culture or reaction
398 medium before each assay. The final DMSO concentrations showed no cytotoxicity. The
399 materials for cell culture were purchased from Thermo Scientific Life Sciences (Grand
400 Island, NY), unless otherwise mentioned.

401 4.2. Cells and Virus

402 African green monkey kidney (Vero, subtype E6) and, human hepatoma (Huh-7), human
403 lung epithelial cell lines (A549 and Calu-3) cells were cultured in high glucose DMEM and
404 human hepatoma lineage (Huh-7) in low glucose DMEM medium, both complemented with
405 10% fetal bovine serum (FBS; HyClone, Logan, Utah), 100 U/mL penicillin and 100 µg/mL
406 streptomycin (Pen/Strep; ThermoFisher) at 37 °C in a humidified atmosphere with 5% CO₂.

407 Human primary monocytes were obtained after 3 h of plastic adherence of peripheral
408 blood mononuclear cells (PBMCs). PBMCs were isolated from healthy donors by density
409 gradient centrifugation (Ficoll-Paque, GE Healthcare). PBMCs (2.0 x 10⁶ cells) were plated
410 onto 48-well plates (NalgeNunc) in RPMI-1640 without serum for 2 to 4 h. Non-adherent
411 cells were removed and the remaining monocytes were maintained in DMEM with 5%

412 human serum (HS; Millipore) and penicillin/streptomycin. The purity of human monocytes
413 was above 95%, as determined by flow cytometric analysis (FACScan; Becton Dickinson)
414 using anti-CD3 (BD Biosciences) and anti-CD16 (Southern Biotech) monoclonal antibodies.

415 NSCs derived from human iPS cells were prepared as previously described[43]. N3D
416 human neurospheres were generated from 3 x 10⁶ NSCs/well in a 6-well plate orbital
417 shaking at 90 rpm and were grown in NEM supplemented with 1xN2 and 1xB27
418 supplements. After 7 days in culture, neurospheres or NSC were infected at MOI 0.1 for 2h
419 at 37 °C. NSCs were washed, neurospheres inoculum were aspirate, and fresh medium
420 containing the compounds was added. Neural cells were observed daily for 5 days after
421 infection. Cell death was measured by tunel approach and virus levels in the supernatant
422 quantified by RT-PCR.

423 SARS-CoV-2 was prepared in Vero E6 cells at MOI of 0.01. Originally, the isolate was
424 obtained from a nasopharyngeal swab from a confirmed case in Rio de Janeiro, Brazil
425 (GenBank #MT710714; Institutional Review Broad approval, 30650420.4.1001.0008). All
426 procedures related to virus culture were handled in a biosafety level 3 (BSL3) multiuser
427 facility according to WHO guidelines. Virus titers were determined as plaque forming units
428 (PFU)/mL. Virus stocks were kept in - 80 °C ultralow freezers.

429 **4.3. Cytotoxicity assay**

430 Monolayers of 1.5 x 10⁴ cells in 96-well plates were treated for 3 days with various
431 concentrations (semi-log dilutions from 1000 to 10 µM) of the antiviral drugs. Then, 5 mg/ml
432 2,3-bis-(2-methoxy-4-nitro-5-sulfophenyl)-2H-tetrazolium-5-carboxanilide (XTT) in
433 DMEM was added to the cells in the presence of 0.01% of N-methyl dibenzopyrazine methyl
434 sulfate (PMS). After incubating for 4 h at 37 °C, the plates were measured in a
435 spectrophotometer at 492 nm and 620 nm. The 50% cytotoxic concentration (CC₅₀) was
436 calculated by a non-linear regression analysis of the dose–response curves.

437 **4.4. Yield-reduction assay**

438 Unless otherwise mentioned, Vero E6 cells were infected with a multiplicity of infection
439 (MOI) of 0.01. HuH-7, A549 and Calu-3 were infected at MOI of 0.1. Cells were infected at
440 densities of 5 x 10⁵ cells/well in 48-well plates for 1h at 37 °C. The NSCs (20 x 10³ cells/well
441 in a 96-well plate) were infected at MOI of 0.1 for 2 h at 37 °C. The cells were washed, and
442 various concentrations of compounds were added to DMEM with 2% FBS. After 24 (Vero
443 E6), or 48h (HuH, -7, A549 and Calu-3) or 5 days (NSCs) supernatants were collected and
444 harvested virus was quantified by PFU/mL or real time RT-PCR. A variable slope non-linear
445 regression analysis of the dose-response curves was performed to calculate the concentration
446 at which each drug inhibited the virus production by 50% (EC₅₀).

447 For time-of-addition assays, 5 x 10⁵ Vero E6 cells/well in 48-well plates were infected
448 with MOI of 0.01 for 1h at 37 °C. Treatments started from 2h before to 18h after infection
449 with two-times EC₅₀ concentration. On the next day, culture supernatants were collected and
450 tittered by PFU/mL.

451

452 **4.5. Virus titration**

453 Monolayers of Vero E6 cells (2×10^4 cell/well) in 96-well plates were infected with serial
454 dilutions of supernatants containing SARS-CoV-2 for 1h at 37°C. Fresh semi-solid medium
455 containing 2.4 % of carboxymethylcellulose (CMC) was added and culture was maintained
456 for 72 h at 37 °C. Cells were fixed with 10 % Formaline for 2 h at room temperature and then,
457 stained with crystal violet (0.4 %). Plaque numbers were scored in at least 3 replicates per
458 dilution by independent readers. The reader was blind with respect to source of the
459 supernatant. The virus titers were determined by plaque-forming units (PFU) per milliliter.

460 **4.6. Molecular detection of virus RNA levels.**

461 The total viral RNA from a culture supernatants and/or monolayers was extracted using
462 QIAamp Viral RNA (Qiagen®), according to manufacturer's instructions. Quantitative RT-
463 PCR was performed using GoTaq® Probe qPCR and RT-qPCR Systems (Promega) in an
464 StepOne™ Real-Time PCR System (Thermo Fisher Scientific) ABI PRISM 7500 Sequence
465 Detection System (Applied Biosystems). Amplifications were carried out in 25 μ L reaction
466 mixtures containing 2 \times reaction mix buffer, 50 μ M of each primer, 10 μ M of probe, and 5
467 μ L of RNA template. Primers, probes, and cycling conditions recommended by the Centers
468 for Disease Control and Prevention (CDC) protocol were used to detect the SARS-CoV-
469 2[44]. The standard curve method was employed for virus quantification. For reference to
470 the cell amounts used, the housekeeping gene RNase P was amplified. The Ct values for this
471 target were compared to those obtained to different cell amounts, 10⁷ to 10², for calibration.
472 Alternatively, genomic (ORF1) and subgenomic (ORFE) were detected, as described
473 elsewhere[45].

474 **4.7. Melting curve assay**

475 The melting profiles were obtained incubating 10 ng of SARS-CoV-2 RNA with 10
476 or 100nM of DCV and Sybergreen (1x) (Thermo Fisher Scientific) in an StepOne™ Real-
477 Time PCR System (Thermo Fisher Scientific) programed with default melting curve. RNA
478 A260/280 ratio was above 1.8, consistent with consistent with high quality material.

479 **4.8. Generation of mutant virus**

480 Vero E6 cells were infected with SARS-CoV-2 at a MOI 0.1 (10-fold higher than
481 used in the pharmacological assays) for 1h at 37 °C and then treated with sub-optimal dose
482 of DCV. Cells were accompanied daily up to the observation of cytopathic effects (CPE).
483 Virus was recovered from the culture supernatant, titered and used in a next round of
484 infection in the presence of higher drug concentration. Concentrations of DCV ranged from
485 0.5 to 7 μ M. As a control, SARS-CoV-2 was also passaged in the absence of treatments to
486 monitor genetic drifts associated with culture. Virus RNA virus was extracted by Qiamp
487 viral RNA (Qiagen) and quantified using Qbit 3 Fluorometer (Thermo Fisher Scientific)
488 according to manufacturers recommendations.

489 The virus RNA was submitted to unbiased sequence using a MGI-2000 and a
490 metatranscriptomics approach. To do so, at least 4.2 ng of purified total RNA of each sample
491 was used for libraries construction using the MGIEasy RNA Library Prep Set (MGI,

492 Shenzhen, China). All libraries were constructed through RNA- fragmentation (250 bp),
493 followed by reverse- transcription and second- strand synthesis. After purification with
494 MGIEasy DNA Clean Beads (MGI, Shenzhen, China), were submitted to end- repair,
495 adaptor- ligation, and PCR amplification steps. After purification as previously described,
496 samples were quantified with Qubit 1X dsDNA HS Assay Kit using an Invitrogen Qubit 4.0
497 Fluorometer (Thermo Fisher Scientific, Foster City, CA) and homogeneously pooled (1
498 pmol/ pool of PCR products) and submitted to denaturation and circularization steps to be
499 transformed into a single- stranded circular DNA library. Purified libraries were quantified
500 with Qubit ssDNA Assay Kit using Invitrogen Qubit 4.0 Fluorometer (Thermo Fisher
501 Scientific, Foster City, CA) and DNA nanoballs were generated by rolling circle
502 amplification of a pool (40 fmol/ reaction), then quantified as described for the libraries and
503 loaded onto the flow cell and sequenced with PE100 (100-bp paired-end reads).

504 Sequencing data were initially analyses in the usegalaxy.org platform. Next, aligned
505 therough clustalW, usina the Mega 7.0 software.

506

507 **4.9. TUNEL (Terminal deoxynucleotidyl transferase-mediated biotinylated UTP Nick 508 End Labelling).**

509 Nuclei from human neurospheres were obtained by isotropic fractionation and plated
510 in 384 plates coated with 0.1 mg/ml poly-L-lysine. Cell death was detected by Apoptag®
511 Red in situ apoptosis detection kit (Merck, catalog # S7165) which labels apoptotic cells,
512 based on staining of 3'-OH termini of DNA strand breaks with rhodamine (red fluorescence),
513 staining was performed according to manufacturer's instructions. Nuclei were labelled with
514 0.5 µg/mL 40-6-diamino-2-phenylindole (DAPI) for 10 minutes. Nuclei were washed with
515 PBS, mounted with glycerol and analyzed in an Operetta high-content imaging system with
516 a 40x objective and high numerical apertures (NA) (PerkinElmer, USA). The data was
517 analyzed using the high-content image analysis software Harmony 5.1 (PerkinElmer, USA).
518 Twelve independent fields were evaluated from duplicate wells per experimental condition.

519 **4.10. Molecular docking**

520 The structures of the active metabolite of SFV and daclatasvir were constructed and
521 optimized by the semi-empirical method RM1, using the Spartan'10 software. The crystal
522 structure of the SARS-CoV-2 nsp12 (PDB code: 7BV2) was extracted from the Protein Data
523 Bank[21].

524 The molecular docking procedure was performed using the Molegro Virtual Docker
525 6.0 software (MVD) [27], which uses a heuristic search algorithm that combines differential
526 evolution with a cavity prediction algorithm. Thus, the MolDock Optimizer search algorithm
527 was used with a minimum of 30 runs, the largest enzyme cavity (1446.4 Å³) was chosen as
528 the center of the search space, and the parameter settings were: population size = 100;
529 maximum iteration = 2000; scaling factor = 0.50; offspring scheme = Scheme 1; termination
530 scheme = variance-based; and crossover rate = 0.90. The complexes of the lowest energy
531 were selected using the rerank scoring function and, then, analyzed also using MVD.

532 **4.11 PBPK model**

533 DCV whole-body PBPK model was constructed in Python 3.5 (in PyCharm 20.1.2
534 (Community edition) using packages – numpy v1.18.5, scipy v1.0.1 and matplotlib v2.1.2)
535 which consists of various compartments representing all the organs and tissues of the body.
536 The drug physicochemical parameters for daclatasvir were presented in supplementary table
537 S1 obtained from various literature sources. The PBPK model was constructed based on few
538 assumptions: 1) uniform and instant distribution across a given tissue, 2) no reabsorption
539 from the colon and 3) the model was blood-flow limited. The simulated data in humans is
540 computer generated, therefore no ethical approval was required for this study.

541 **4.12. Model development**

542 The model was simulated using a population of one hundred virtual healthy
543 individuals (50% female) between 20-60 years and having weight and height as provided by
544 the US national health statistics reports[46]. Organ weights and volumes, blood flow rates
545 were obtained using anthropometric equations from literature[47,48] and the characteristics
546 such as weight and height from US statistics[46]. A seven compartmental absorption and
547 transit model representing the various parts of the duodenum, jejunum and ileum to capture
548 effective absorption kinetics was used in the model. The drug was assumed to have entire
549 administered dose in solution for absorption and completely depend on the rate kinetics
550 involved during this process. Effective permeability of daclatasvir was scaled from apparent
551 permeability from PAMPA (due to lack of available data, it was assumed the same in Caco-
552 2 cells) using the *in vitro – in vivo* extrapolation[49,50] to compute the absorption rate from
553 the small intestine.

554 The volume of distribution was computed using the tissue to plasma ratios computed
555 from Rogers & Rowland [51] and a tissue to plasma partition factor (K_p factor) of 0.025 was
556 used to adjust the volume of distribution to the literature value of 47 L[52]. A population of
557 100 individuals was simulated by varying the mean values with available standard deviation
558 for each of the parameters in the model such that every simulation represents a unique
559 individual.

560 **4.13. Model validation**

561 DCV PBPK model was validated in healthy individuals using available data in
562 humans for various single doses – 1, 10, 25, 50, 100 and 200 mg and for various multiple
563 doses – 1, 10, 30 and 60 mg at fasted state. Clinical data was digitised using Web Plot
564 Digitiser® software from available plots. The model was considered validated when: 1)
565 closeness of the simulated points to the literature data computed using absolute average fold
566 error (AAFE) between the simulated and observed plasma concentration – time points was
567 less than two; and 2) the mean simulated pharmacokinetic parameters - maximum
568 concentration (C_{max}) and the area under the plasma concentration-time curve (AUC) were
569 less than two-fold from mean observed values.

570 **4.14. Model simulations**

571 For the inhibition of SARS-CoV-2, a mean target concentration (EC₉₀) of 4.12 μ M or
572 3079 ng/ml obtained from multiple *in vitro* studies was used [53]. Optimal dosing regimen
573 for treatment of SARS-CoV-2 was identified from various BID and TID dosing regimens
574 such that at least 90% of the simulated population have trough plasma concentration at 24 h
575 (C₂₄) over the mean target concentration with a low overall total dose per day.

576 **4.15. Ethics Statement**

577 Experimental procedures involving human cells from healthy donors were performed
578 with samples obtained after written informed consent and were approved by the Institutional
579 Review Board (IRB) of the Oswaldo Cruz Foundation/Fiocruz (Rio de Janeiro, RJ, Brazil)
580 under the number 397-07. The National Review Board approved the study protocol (CONEP
581 30650420.4.1001.0008), and informed consent was obtained from all participants or patients'
582 representatives.

583 **4.16. Statistical analysis**

584 The assays were performed blinded by one professional, codified and then read by
585 another professional. All experiments were carried out at least three independent times,
586 including a minimum of two technical replicates in each assay. The dose-response curves
587 used to calculate EC₅₀ and CC₅₀ values were generated by variable slope plot from Prism
588 GraphPad software 8.0. The equations to fit the best curve were generated based on R² values
589 ≥ 0.9 . Student's T-test was used to access statistically significant *P* values <0.05 . The
590 statistical analyses specific to each software program used in the bioinformatics analysis are
591 described above.

592 **Acknowledgments**

593 Thanks are due to Prof. Andrew Hill from the University of Liverpool and Dr. James Freeman
594 from the GP2U Telehealth for simulative scientific debate. Dr. Carmen Beatriz Wagner
595 Giacoia Gripp from Oswaldo Cruz Institute is acknowledged for assessments related to BSL3
596 facility. Dr. Andre Sampaio from Farmanguinhos, platform RPT11M, is acknowledged for
597 kindly donate the Calu-3. We thank the Hemotherapy Service of the Hospital Clementino
598 Fraga Filho (Federal University of Rio de Janeiro, Brazil) for providing buffy-coats. This
599 work was supported by Conselho Nacional de Desenvolvimento Científico e Tecnológico
600 (CNPq), Fundação de Amparo à Pesquisa do Estado do Rio de Janeiro (FAPERJ). This study
601 was financed in part by the Coordenação de Aperfeiçoamento de Pessoal de Nível Superior
602 - Brasil (CAPES) - Finance Code 001. Funding was also provided by CNPq, CAPES and
603 FAPERJ through the National Institutes of Science and Technology Program (INCT) to
604 Carlos Morel (INCT-IDPN). Thanks are due to Oswaldo Cruz Foundation/FIOCRUZ under
605 the auspicious of Inova program (B3-Bovespa funding). The funding sponsors had no role in
606 the design of the study; in the collection, analyses, or interpretation of data; in the writing of
607 the manuscript, and in the decision to publish the results.

608

609

610 **References**

- 611 1. Cui J, Li F, Shi Z-L. Origin and evolution of pathogenic coronaviruses. *Nat Rev Microbiol.* 612 2019;17: 181–192. doi:10.1038/s41579-018-0118-9
- 613 2. Dong E, Du H, Gardner L. An interactive web-based dashboard to track COVID-19 in real time. 614 *The Lancet Infectious Diseases.* 2020;0. doi:10.1016/S1473-3099(20)30120-1
- 615 3. Organization WH. WHO R&D Blueprint: informal consultation on prioritization of candidate 616 therapeutic agents for use in novel coronavirus 2019 infection, Geneva, Switzerland, 24 617 January 2020. 2020 [cited 29 Mar 2020]. Available: 618 <https://apps.who.int/iris/handle/10665/330680>
- 619 4. Borba MGS, Val FFA, Sampaio VS, Alexandre MAA, Melo GC, Brito M, et al. Effect of High vs 620 Low Doses of Chloroquine Diphosphate as Adjunctive Therapy for Patients Hospitalized With 621 Severe Acute Respiratory Syndrome Coronavirus 2 (SARS-CoV-2) Infection: A Randomized 622 Clinical Trial. *JAMA Netw Open.* 2020;3: e208857–e208857. 623 doi:10.1001/jamanetworkopen.2020.8857
- 624 5. Wang Y, Zhang D, Du G, Du R, Zhao J, Jin Y, et al. Remdesivir in adults with severe COVID-19: 625 a randomised, double-blind, placebo-controlled, multicentre trial. *The Lancet.* 2020;395: 626 1569–1578. doi:10.1016/S0140-6736(20)31022-9
- 627 6. Cao B, Wang Y, Wen D, Liu W, Wang J, Fan G, et al. A Trial of Lopinavir-Ritonavir in Adults 628 Hospitalized with Severe Covid-19. *N Engl J Med.* 2020. doi:10.1056/NEJMoa2001282
- 629 7. Goldman JD, Lye DCB, Hui DS, Marks KM, Bruno R, Montejano R, et al. Remdesivir for 5 or 10 630 Days in Patients with Severe Covid-19. *New England Journal of Medicine.* 2020;0: null. 631 doi:10.1056/NEJMoa2015301
- 632 8. Beigel JH, Tomashek KM, Dodd LE, Mehta AK, Zingman BS, Kalil AC, et al. Remdesivir for the 633 Treatment of Covid-19 — Preliminary Report. *New England Journal of Medicine.* 2020;0: null. 634 doi:10.1056/NEJMoa2007764
- 635 9. De Clercq E, Li G. Approved Antiviral Drugs over the Past 50 Years. *Clin Microbiol Rev.* 636 2016;29: 695–747. doi:10.1128/CMR.00102-15
- 637 10. Smith MA, Regal RE, Mohammad RA. Daclatasvir: A NS5A Replication Complex Inhibitor for 638 Hepatitis C Infection. *Ann Pharmacother.* 2016;50: 39–46. doi:10.1177/1060028015610342
- 639 11. Gordon DE, Jang GM, Bouhaddou M, Xu J, Obernier K, O'Meara MJ, et al. A SARS-CoV-2- 640 Human Protein-Protein Interaction Map Reveals Drug Targets and Potential Drug- 641 Repurposing. *bioRxiv.* 2020; 2020.03.22.002386. doi:10.1101/2020.03.22.002386
- 642 12. Keating GM. Sofosbuvir: a review of its use in patients with chronic hepatitis C. *Drugs.* 643 2014;74: 1127–1146. doi:10.1007/s40265-014-0247-z
- 644 13. de Freitas CS, Higa LM, Sacramento CQ, Ferreira AC, Reis PA, Delvecchio R, et al. Yellow fever 645 virus is susceptible to sofosbuvir both in vitro and in vivo. *PLoS Negl Trop Dis.* 2019;13: 646 e0007072. doi:10.1371/journal.pntd.0007072

647 14. Ferreira AC, Reis PA, de Freitas CS, Sacramento CQ, Villas Boas Hoelz L, Bastos MM, et al.
648 Beyond members of the Flaviviridae family, sofosbuvir also inhibits chikungunya virus
649 replication. *Antimicrob Agents Chemother*. 2018. doi:10.1128/aac.01389-18

650 15. Ferreira AC, Zaverucha-do-Valle C, Reis PA, Barbosa-Lima G, Vieira YR, Mattos M, et al.
651 Sofosbuvir protects Zika virus-infected mice from mortality, preventing short- and long-term
652 sequelae. *Scientific Reports*. 2017;7: 9409. doi:doi:10.1038/s41598-017-09797-8

653 16. Sacramento CQ, de Melo GR, de Freitas CS, Rocha N, Hoelz LV, Miranda M, et al. The
654 clinically approved antiviral drug sofosbuvir inhibits Zika virus replication. *Sci Rep*. 2017;7:
655 40920. doi:10.1038/srep40920

656 17. SOVALDI (sofosbuvir). : 37.

657 18. Tissue expression of CTSA - Staining in lung - The Human Protein Atlas. [cited 15 Jun 2020].
658 Available: <https://www.proteinatlas.org/ENSG00000064601-CTSA/tissue/lung>

659 19. Tissue expression of CES1 - Summary - The Human Protein Atlas. [cited 15 Jun 2020].
660 Available: <https://www.proteinatlas.org/ENSG00000198848-CES1/tissue>

661 20. Tissue expression of HINT1 - Summary - The Human Protein Atlas. [cited 15 Jun 2020].
662 Available: <https://www.proteinatlas.org/ENSG00000169567-HINT1/tissue>

663 21. Gao Y, Yan L, Huang Y, Liu F, Zhao Y, Cao L, et al. Structure of the RNA-dependent RNA
664 polymerase from COVID-19 virus. *Science*. 2020;368: 779–782. doi:10.1126/science.abb7498

665 22. Gordon CJ, Tchesnokov EP, Woolner E, Perry JK, Feng JY, Porter DP, et al. Remdesivir is a
666 direct-acting antiviral that inhibits RNA-dependent RNA polymerase from severe acute
667 respiratory syndrome coronavirus 2 with high potency. *J Biol Chem*. 2020; jbc.RA120.013679.
668 doi:10.1074/jbc.RA120.013679

669 23. Ju J, Kumar S, Li X, Jockusch S, Russo JJ. Nucleotide Analogues as Inhibitors of Viral
670 Polymerases. *bioRxiv*. 2020; 2020.01.30.927574. doi:10.1101/2020.01.30.927574

671 24. Mesci P, Macia A, Saleh A, Martin-Sancho L, Yin X, Snethlage C, et al. Sofosbuvir protects
672 human brain organoids against SARS-CoV-2. *bioRxiv*. 2020; 2020.05.30.125856.
673 doi:10.1101/2020.05.30.125856

674 25. Asadi-Pooya AA, Simani L. Central nervous system manifestations of COVID-19: A systematic
675 review. *J Neurol Sci*. 2020;413: 116832. doi:10.1016/j.jns.2020.116832

676 26. Zhou F, Yu T, Du R, Fan G, Liu Y, Liu Z, et al. Clinical course and risk factors for mortality of
677 adult inpatients with COVID-19 in Wuhan, China: a retrospective cohort study. *The Lancet*.
678 2020;395: 1054–1062. doi:10.1016/S0140-6736(20)30566-3

679 27. Thomsen R, Christensen MH. MolDock: a new technique for high-accuracy molecular
680 docking. *J Med Chem*. 2006;49: 3315–3321. doi:10.1021/jm051197e

681 28. Rangan R, Zheludev IN, Hagey RJ, Pham EA, Wayment-Steele HK, Glenn JS, et al. RNA genome
682 conservation and secondary structure in SARS-CoV-2 and SARS-related viruses: a first look.
683 *RNA*. 2020;26: 937–959. doi:10.1261/rna.076141.120

684 29. Arshad U, Pertinez H, Box H, Tatham L, Rajoli RKR, Curley P, et al. Prioritization of Anti-SARS-
685 Cov-2 Drug Repurposing Opportunities Based on Plasma and Target Site Concentrations
686 Derived from their Established Human Pharmacokinetics. *Clin Pharmacol Ther.* 2020.
687 doi:10.1002/cpt.1909

688 30. Zeitlinger M, Koch BCP, Bruggemann R, De Cock P, Felton T, Hites M, et al. Pharmacokinetics/Pharmacodynamics of Antiviral Agents Used to Treat SARS-CoV-2 and
689 Their Potential Interaction with Drugs and Other Supportive Measures: A Comprehensive
690 Review by the PK/PD of Anti-Infectives Study Group of the European Society of Antimicrobial
691 Agents. *Clin Pharmacokinet.* 2020. doi:10.1007/s40262-020-00924-9

692 693 31. Venisse N, Peytavin G, Bouchet S, Gagnieu M-C, Garraffo R, Guilhaumou R, et al. Concerns
694 about pharmacokinetic (PK) and pharmacokinetic-pharmacodynamic (PK-PD) studies in the
695 new therapeutic area of COVID-19 infection. *Antiviral Res.* 2020; 104866.
696 doi:10.1016/j.antiviral.2020.104866

697 698 32. Alexander SPH, Armstrong JF, Davenport AP, Davies JA, Faccenda E, Harding SD, et al. A
699 rational roadmap for SARS-CoV-2/COVID-19 pharmacotherapeutic research and
development: IUPHAR Review 29. *Br J Pharmacol.* 2020. doi:10.1111/bph.15094

700 701 33. Dong E, Du H, Gardner L. An interactive web-based dashboard to track COVID-19 in real time. *The Lancet Infectious Diseases.* 2020;0. doi:10.1016/S1473-3099(20)30120-1

702 703 34. Lin L, Lu L, Cao W, Li T. Hypothesis for potential pathogenesis of SARS-CoV-2 infection-a
704 review of immune changes in patients with viral pneumonia. *Emerg Microbes Infect.* 2020;9:
727–732. doi:10.1080/22221751.2020.1746199

705 706 35. Li H, Liu L, Zhang D, Xu J, Dai H, Tang N, et al. SARS-CoV-2 and viral sepsis: observations and
hypotheses. *The Lancet.* 2020;395: 1517–1520. doi:10.1016/S0140-6736(20)30920-X

707 708 36. Wang Y, Liu S, Liu H, Li W, Lin F, Jiang L, et al. SARS-CoV-2 infection of the liver directly
709 contributes to hepatic impairment in patients with COVID-19. *J Hepatol.* 2020.
doi:10.1016/j.jhep.2020.05.002

710 711 37. Harrison C. Coronavirus puts drug repurposing on the fast track. *Nat Biotechnol.* 2020.
doi:10.1038/d41587-020-00003-1

712 713 38. Figueiredo-Mello C, Casadio LVB, Avelino-Silva VI, Yeh-Li H, Sztajnbok J, Joelsons D, et al.
714 Efficacy of sofosbuvir as treatment for yellow fever: protocol for a randomised controlled
715 trial in Brazil (SOFFA study). *BMJ Open.* 2019;9: e027207. doi:10.1136/bmjopen-2018-
027207

716 717 39. Pruijssers AJ, George AS, Schäfer A, Leist SR, Gralinski LE, Dinnon KH, et al. Remdesivir
718 Inhibits SARS-CoV-2 in Human Lung Cells and Chimeric SARS-CoV Expressing the SARS-CoV-2
RNA Polymerase in Mice. *Cell Rep.* 2020;32: 107940. doi:10.1016/j.celrep.2020.107940

719 720 40. Murphy BG, Perron M, Murakami E, Bauer K, Park Y, Eckstrand C, et al. The nucleoside
721 analog GS-441524 strongly inhibits feline infectious peritonitis (FIP) virus in tissue culture
722 and experimental cat infection studies. *Vet Microbiol.* 2018;219: 226–233.
doi:10.1016/j.vetmic.2018.04.026

723 41. Yan VC, Muller FL. Advantages of the Parent Nucleoside GS-441524 over Remdesivir for
724 Covid-19 Treatment. ACS Med Chem Lett. 2020;11: 1361–1366.
725 doi:10.1021/acsmedchemlett.0c00316

726 42. HCV drugs sofosbuvir, daclatasvir show promise as potential COVID-19 treatment. [cited 28
727 Jul 2020]. Available: <https://www.healio.com/news/infectious-disease/20200709/hcv-drugs-sofosbuvir-daclatasvir-show-promise-as-potential-covid19-treatment>

729 43. Garcez PP, Loiola EC, Madeiro da Costa R, Higa LM, Trindade P, Delvecchio R, et al. Zika virus
730 impairs growth in human neurospheres and brain organoids. Science. 2016;352: 816–818.
731 doi:10.1126/science.aaf6116

732 44. CDC. Coronavirus Disease 2019 (COVID-19). In: Centers for Disease Control and Prevention
733 [Internet]. 11 Feb 2020 [cited 30 Mar 2020]. Available:
734 <https://www.cdc.gov/coronavirus/2019-ncov/lab/rt-pcr-panel-primer-probes.html>

735 45. Wölfel R, Corman VM, Guggemos W, Seilmaier M, Zange S, Müller MA, et al. Virological
736 assessment of hospitalized patients with COVID-2019. Nature. 2020;581: 465–469.
737 doi:10.1038/s41586-020-2196-x

738 46. National Health Statistics Reports, Number 122, December 20, 2018. 2018; 16.

739 47. Bosgra S, van Eijkeren J, Bos P, Zeilmaker M, Slob W. An improved model to predict
740 physiologically based model parameters and their inter-individual variability from
741 anthropometry. Crit Rev Toxicol. 2012;42: 751–767. doi:10.3109/10408444.2012.709225

742 48. Williams LR. Reference values for total blood volume and cardiac output in humans. Oak
743 Ridge National Lab., TN (United States); 1994 Sep. Report No.: ORNL/TM-12814.
744 doi:10.2172/10186900

745 49. Sun D, Lennernas H, Welage LS, Barnett JL, Landowski CP, Foster D, et al. Comparison of
746 human duodenum and Caco-2 gene expression profiles for 12,000 gene sequences tags and
747 correlation with permeability of 26 drugs. Pharm Res. 2002;19: 1400–1416.
748 doi:10.1023/a:1020483911355

749 50. Gertz M, Harrison A, Houston JB, Galetin A. Prediction of human intestinal first-pass
750 metabolism of 25 CYP3A substrates from in vitro clearance and permeability data. Drug
751 Metab Dispos. 2010;38: 1147–1158. doi:10.1124/dmd.110.032649

752 51. Rodgers T, Rowland M. Physiologically based pharmacokinetic modelling 2: predicting the
753 tissue distribution of acids, very weak bases, neutrals and zwitterions. J Pharm Sci. 2006;95:
754 1238–1257. doi:10.1002/jps.20502

755 52. Daclatasvir. [cited 28 Jul 2020]. Available: <https://www.drugbank.ca/drugs/DB09102>

756 53. Wang Q, Li W, Zheng M, Eley T, LaCreta F, Garimella T. Physiologically-Based Simulation of
757 Daclatasvir Pharmacokinetics With Antiretroviral Inducers and Inhibitors of Cytochrome P450
758 and Drug Transporters. : 14.

759
760 **Author contributions**
761

762 Experimental execution and analysis – CQS, NFR, JRT, SSGD, APDDS, CSS, ACF, MM,
763 CRRP, CSF, VCS, FBS, MAF, CSGP, GV, LRQS, LGS, LVBH, TVAF, FSCB, MMB,
764 RKRR

765 Data analysis, manuscript preparation and revision – CQS, NFR, JRT, MZPG NB, FAB, AO,
766 MZG, SKR, DCBH, PTB, TMLS

767 Conceptualized the experiments – CQS, NFR, JRT, TMLS

768 Study coordination – TMLS

769 Manuscript preparation and revision – DCBH, PTB, TMLS

770

771

772 **The authors declare no competing financial interests.**

773

774

775

776

777

778

779

780

781

782

783

784

785

786

787

788

789

790

791

792

793

794 **Table 1 – The pharmacological parameters of SARS-CoV-2 infected cell in the presence**
795 **of DCV and SFV**

Drugs	Vero			Huh-7			Calu-3		
	EC50	CC50	SI	EC50	CC50	SI	EC50	CC50	SI
DCV	0.8 ± 0.3	31 ± 8	39	0.6 ± 0.2	28 ± 5	47	1.1 ± 0.3	38 ± 5	34
SFV	>10	360 ± 43	ND	5.1 ± 0.8	381 ± 34	74	7.3 ± 0.5	512 ± 34	70
GS-331007	>10	512± 24	ND	>10	421 ± 18	ND	9.3 ± 0.2	630 ± 34	68
DCV/SFV	ND	ND	ND	ND	ND	ND	0.7 ± 0.2	389 ± 12	555
RBV	ND	ND	ND	6.5 ± 1.3	142 ± 12	13	7.1 ± 0.5	160	16
CQ	1.3 ± 0.4	268 ± 23	206	ND	ND	ND	ND	ND	ND
LPV/RTV	5.3 ± 0.5	291 ± 32	54	2.9 ± 0.2	328 ± 16	113	8.2 ± 0.3	256 ± 17	31

796 EC₅₀, and CC₅₀ are described in μM

797 DCV – daclatasvir, SFV – sofovabuvir, GS-331007 – SFV's nucleoside, RBV – ribavirin, CQ
798 – Chloroquine, LPV/RTV – lopinavir/ritonavir

799

800

801

802

803

804

805

806

807

808

809

810

811

812

813

814

815

816 **Table 2 – Genetic and biochemical characteristics of the DCV- mutant SARS-
817 CoV-2.
818**

Mutations in red. Insertions in bold

831 **Legend for the Figures**

832 **Figure 1. The antiviral activity of daclatasvir (DCV) and sofosbuvir (SFV) against**
833 **SARS-CoV-2.** Vero (A and D), HuH-7 (B and E) or Calu-3 (C and F) cells, at density of 5×10^5 cells/well in 48-well plates, were infected with SARS-CoV-2, for 1h at 37 °C. Inoculum
834 was removed, cells were washed and incubated with fresh DMEM containing 2% fetal bovine
835 serum (FBS) and the indicated concentrations of the DCV, SFV, chloroquine (CQ),
836 lopinavir/ritonavir (LPV+RTV) or ribavirin (RBV). Vero (A and D) were infected with MOI
837 of 0.01 and supernatants were accessed after 24 h. HuH-7 (B and E) and Calu-3 (C and F)
838 cells were infected with MOI of 0.1 and supernatants were accessed after 48 h. Viral
839 replication in the culture supernatant was measured by PFU/mL. Results are displayed as
840 percentage of inhibition (A-C) or virus titers (D-F). The data represent means \pm SEM of three
841 independent experiments.

843 **Figure 2. Sofosbuvir (SFV) inhibits SARS-CoV-2 replication in human iPS cell-derived**
844 **NSCs.** (A) NSCs were infected at MOIs of 0.1 and treated with 1 μ M of SFV or daclatasvir
845 (DCV). After 5 days, the culture supernatants were collected, and the virus was quantified
846 by RNA levels using RT-PCR. (B) NSCs in spheroid format were labeled for Tunel and
847 DAPI after 5 days post-infection. The data represent means \pm SEM of three independent
848 experiments. * indicates $P < 0.05$ for the comparison between the SARS-CoV-2-infected
849 cells untreated (nil) vs treated with SFV.

850
851 **Figure 3. Daclatasvir (DCV) impairs SARS-CoV-2 replication and cytokine storm in**
852 **human primary monocytes.** Human primary monocytes were infected at the MOI of 0.01
853 and treated with 1 μ M of daclatasvir (DCV) sofosbuvir (SFV), chloroquine (CQ), atazanavir
854 (ATV) or atazanavir/ritonavir (ATV+RTV). After 24h, cell-associated virus RNA loads (A),
855 as well as TNF- α (B) and IL-6 (C) levels in the culture supernatant were measured. The data
856 represent means \pm SEM of experiments with cells from at least three healthy donors.
857 Differences with $P < 0.05$ are indicated (*), when compared to untreated cells (nil) to each
858 specific treatment.

859
860 **Figure 4. Daclatasvir (DCV) and sofosbuvir (SFV) reduced SARS-CoV-2 associated**
861 **RNA synthesis.** (A) To initially understand the temporal pattern of inhibition promoted
862 daclatasvir, we performed by Time-of-addition assays. Vero cells were infected with MOI of
863 0.01 of SARS-CoV-2 and treated with daclatasvir or ribavirin (RBV) with two-times their
864 EC₅₀ values at different times after infection, as indicated. After 24h post infection, culture
865 supernatant was harvested and SARS-CoV-2 replication measured by plaque assay. (B) Next,
866 Calu-3 cells (5×10^5 cells/well in 48-well plates), were infected with SARS-CoV-2 at MOI
867 of 0.1, for 1h at 37 °C. Inoculum was removed, cells were washed and incubated with fresh
868 DMEM containing 2% fetal bovine serum (FBS) and the indicated concentrations of the
869 daclatasvir, SFV or ribavirin (RBV) at 10 μ M. After 48h, cells monolayers were lysed, total
870 RNA extracted and quantitative RT-PCR performed for detection of ORF1 and ORF1b
871 mRNA. The data represent means \pm SEM of three independent experiments. * $P < 0.05$ for
872 comparisons with vehicle (DMSO). # $P < 0.05$ for differences in genomic and sub-genomic
873 RNA.

874 **Figure 5.** (A) Cartoon representation of SARS-CoV-2 RNA polymerase (nsp12; blue) with
875 RNA template (yellow), and Mg²⁺ (pink) ions, in CPK representation, complexed to the
876 active metabolite of sofosbuvir (SFV; red) (A) and daclatasvir (B). Schematic representations
877 of the hydrogen bonds (H-bonds; blue dashed lines), attractive electrostatic interactions (red
878 dashed lines), and steric interactions (green dashed lines) present in the nsp12-SFV (C) and
879 nsp12-daclatasvir (D) complexes. The nsp12 residues, RNA nucleotides, and Mg²⁺ ions are
880 represented by white, yellow, and orange rectangles.

881

882 **Figure 6. Daclatasvir (DCV) favors SARS-CoV-2 RNA unfold.** A total of 10 ng of SARS-
883 CoV-2 RNA was incubated with 10 or 100 nM of DCV during a standard melting curve in
884 the presence of picogreen, derivative (A) and normalized (B) reports are presented. (C) the
885 scheme represent the percentage of wild-type (WT; white) and mutant (black) virus after
886 growing SARS-CoV-2 in Vero Cells at a MOI 10 times higher than used in other
887 experiments, 0.1, and sequentially treated with sub-optimal doses of DCV. Each passage was
888 done after 2-4 days pos-infection, when cytopathic effect was evident. Virus RNA was
889 unbiased sequenced using a MGI-2000 and a metatrasncriptomic approach was employed
890 during the analysis. WT (D) and mutant (E) SARS-CoV-2 secondary RNA structure
891 encompassing the nucleotides 28169-28259 are presented.

892

893 **Figure 7 - Predicted daclatasvir plasma concentration for multiple 60 mg and 330 mg**
894 **TID doses.** The dotted and the dashed lines represent the EC₉₀ and EC₅₀ values of
895 daclatasvir for SARS-CoV-2.

896

897

898

899

900

901

902

903

904

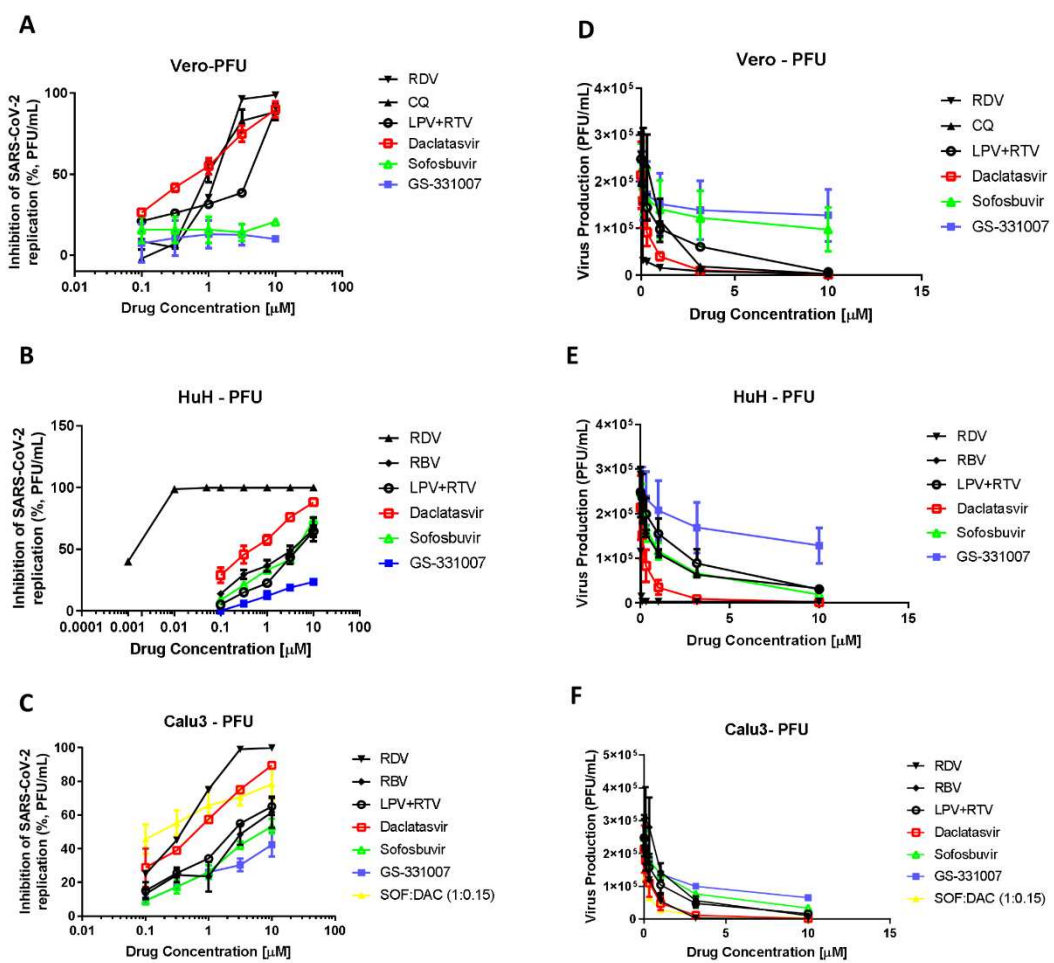
905

906

907

908

909 Figure 1



910

911

912

913

914

915

916

917

918

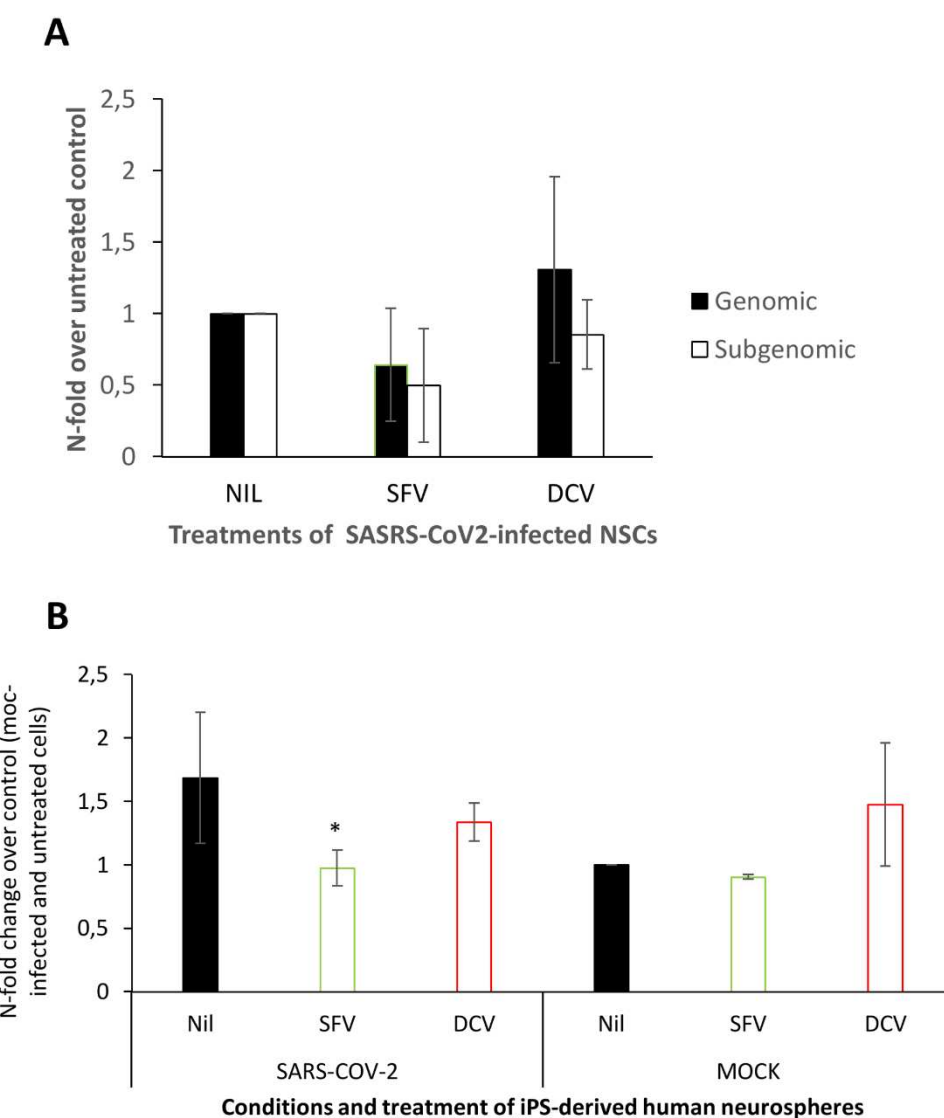
919

920

921

922

923 Figure 2



924

925

926

927

928

929

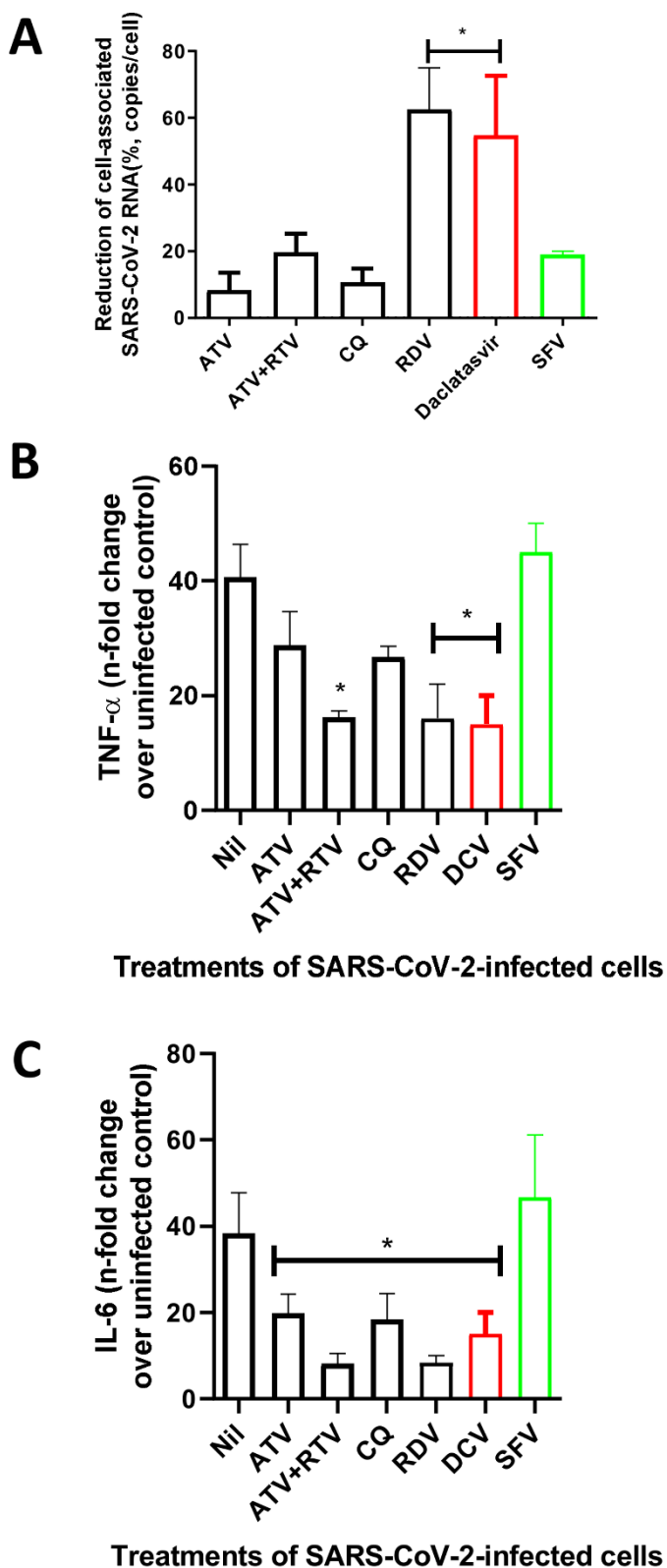
930

931

932

933

934 Figure 3

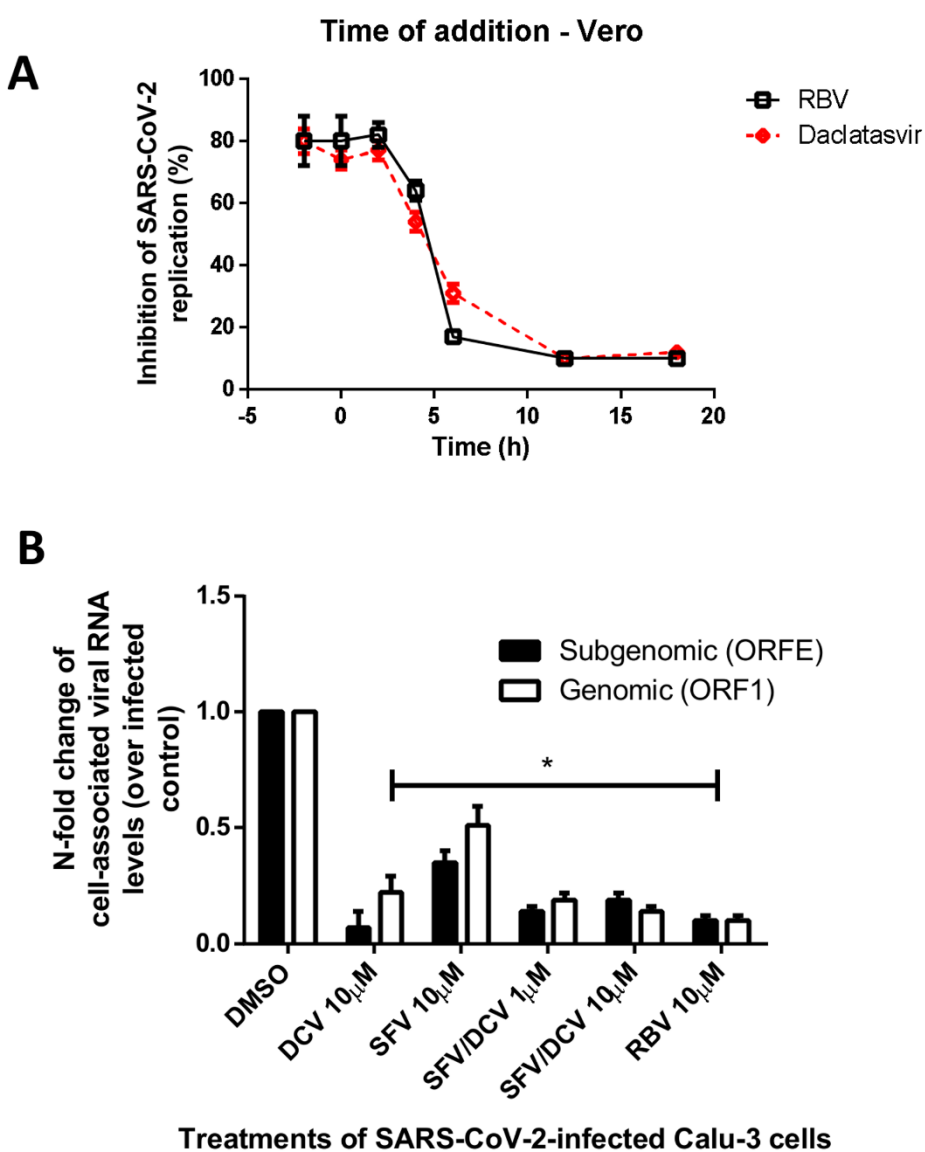


935

936

937

938 Figure 4



939

940

941

942

943

944

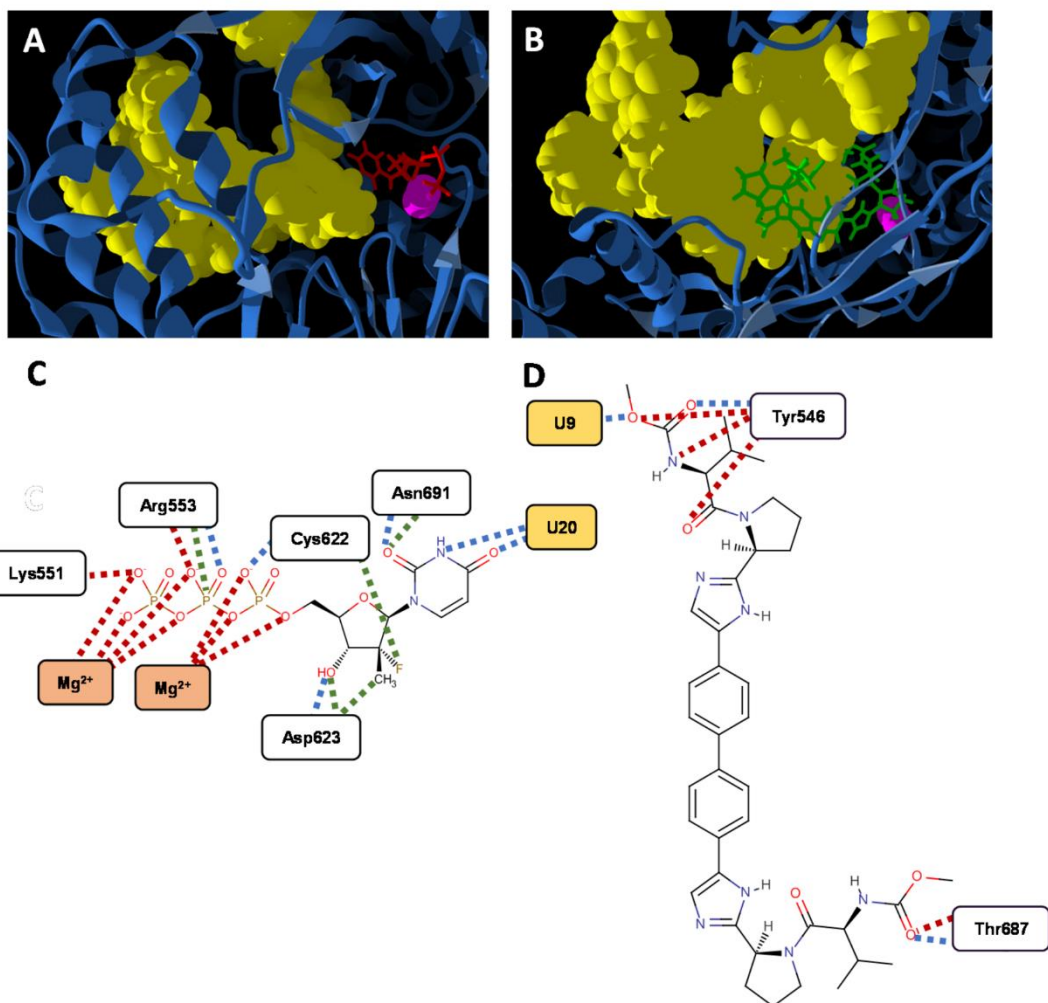
945

946

947

948

949 Figure 5



950

951

952

953

954

955

956

957

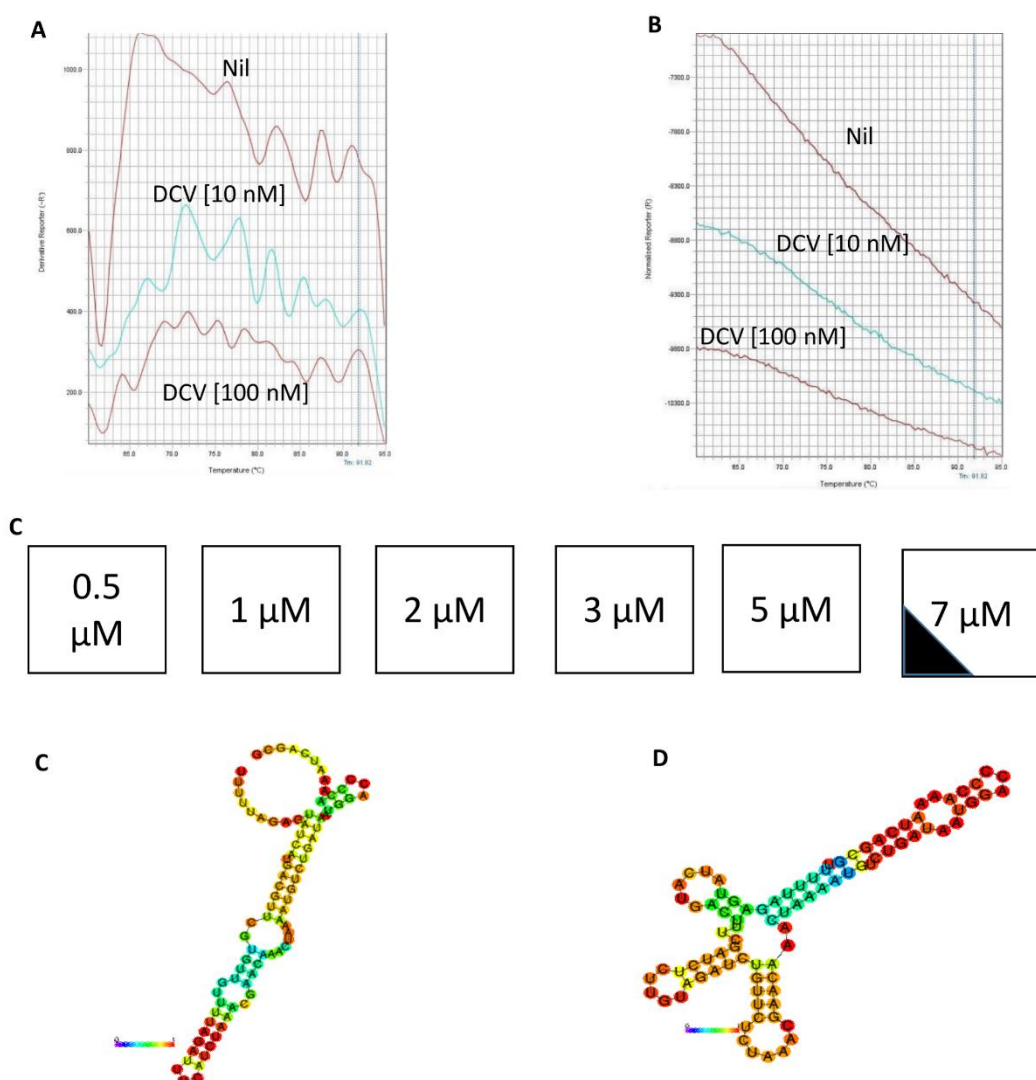
958

959

960

961

962 Figure 6



963

964

965

966

967

968

969

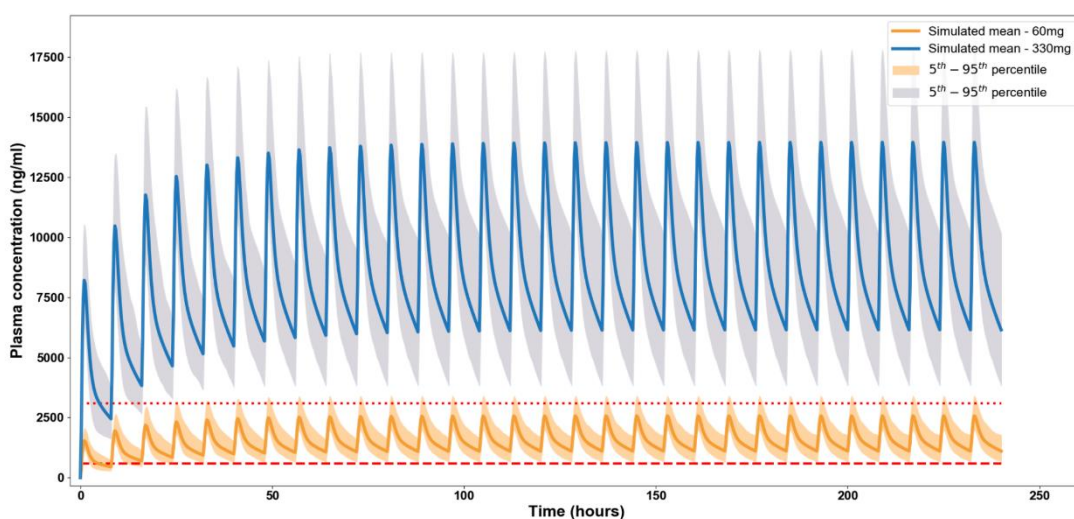
970

971

972

973

974 Figure 7



975

976

977

978

979

980

981

982

983

984

985

986

987

988

989

990

991

992

993

994